Structural and magnetic properties of MBE-grown GeMnN_{2} thin films

Y. Liu, V. K. Lazarov, S. H. Cheung, D. J. Keavney, Z. Gai, M. Gajdardziska-Josifovska, M. Weinert, and L. Li

Phys. Rev. B **85**, 144113 — Published 23 April 2012

DOI: 10.1103/PhysRevB.85.144113

Structural and magnetic properties of MBE grown $GeMnN_2$ thin films

Y. Liu[1], V. K. Lazarov[1,2], S. H. Cheung[1], D. J. Keavney[3], Z. Gai[4], M. Gajdardziska-Josifovska[1], M. Weinert[1], and L. Li[1*]

[1]Physics Department, University of Wisconsin, Milwaukee, WI 53211

[2]Department of Physics, University of York, York YO10 5DD, UK

[3]Advanced Photon Source, Argonne National Laboratory, Argonne, IL 60439

[4]Center for Nanophase Materials Sciences, Oak Ridge National Laboratory, Oak Ridge, TN 37831

Abstract:

Epitaxial $GeMnN_2$ thin films are synthesized by plasma-assisted molecular beam epitaxy. Transmission electron microscopy and x-ray diffraction measurements confirm that it is the orthorhombic variant, consistent with the predictions of first-principles calculations. The magnetic properties of the films are related to defects, with samples grown under Ge-rich conditions exhibiting a net magnetic moment above room temperature. These results are explained by first-principles calculations, indicating that the preferential substitution of one magnetic sublattice of $GeMnN_2$ by impurities and/or intrinsic defects such as Ge antisites produces a net magnetic moment in an antiferromagnetic background and also introduces spin-polarized carriers near the Fermi level.

PACS numbers: 75.50.Pp, 71.15.Mb, 81.15.Hi, 68.37.Lp

*Electronic address: lianli@uwm.edu

I. Introduction

Research in magnetic semiconductors is fueled largely by the prospect of building all-semiconductor-based spin devices[1,2]. The most common avenue to synthesize these materials is to dope a semiconductor host with a transition-metal such as Mn during chemical vapor phase deposition or molecular beam epitaxy (MBE)[3,4]. In the case of III-V semiconductors, the substitution of the group III atom with a Mn simultaneously provides a localized magnetic moment and a hole. With the exchange interaction amongst the localized *d* electrons of Mn mediated by the holes, ferromagnetic ordering can be realized, leading to diluted *p*-type ferromagnetic semiconductors[3,4]. The challenge here is overcome the solubility limits of transition metals in these semiconductor hosts to achieve room temperature Curie temperature[5-9]. In chalcopyrite II-IV-V_2 semiconductors that are isovalent to III-V's, where the average valence of the group II and IV atoms is equivalent to that of group III[10], isovalent substitution of the group II site by transition metal ions (e.g., Mn^{2+} ions) would accommodate much higher concentrations[11]. However, simple superexchange arguments suggest that such an arrangement should lead to antiferromagnetic (AFM) coupling. Nevertheless, interactions between Mn and hole-producing intrinsic defects can lead to ferromagnetic ordering[12]. While significant progress has been made using these methods, the materials produced often exhibit T_C lower than room temperature, and the carrier type cannot be independently controlled (e.g., *p*-type for Mn-doped GaAs[3,4]).

In this work, we explore the avenue of selective doping of an antiferromagnetically ordered semiconductor $GeMnN_2$ towards the creation of a magnetic semiconductor. We have synthesized a series of epitaxial $GeMnN_2$ films by electron-cyclotron resonance plasma-assisted MBE. Structural characterization by x-ray diffraction (XRD), high-resolution transmission electron microscopy (HRTEM), and convergent beam electron diffraction (CBED) indicate that the

$GeMnN_2$ film is the orthorhombic variant, consistent with first-principles calculations. Magnetic properties measured by soft x-ray absorption spectroscopy (XAS), magnetic circular dichoism (XMCD), and Quantum Design magnetic property measurement system (MPMS) indicate that the magnetic properties of the films are related to defects, with samples grown under Ge-rich conditions exhibiting a net magnetic moment above room temperature. These results are explained by first-principles calculations, which show that the preferential substitution of one magnetic sublattice of $GeMnN_2$ by impurities and/or intrinsic defects such as Ge antisites on one of its sublattices induces a net *ferri*magnetic moment in an antiferromagnetic background. In addition, different dopants/impurities place the impurity states and the Fermi level at different positions in the gap, making both *n*- and *p*-type doping possible, essential for magnetic semiconductor based spin devices.

II. Methods

The $GeMnN_2$ films were grown on 6H-SiC(0001), Al_2O_3(0001), and MgO(111) substrates using electron-cyclotron-resonance plasma-assisted MBE. The details of the substrate preparation and the MBE system are described elsewhere[13,14]. A 30 nm GaN buffer layer was first grown at 570 °C with a Ga effusion cell temperature of 950 °C, nitrogen flow rate of 3.0 to 4.0 sccm and plasma power of 30 W. Thin films of $GeMnN_2$ were subsequently deposited at a reduced substrate temperature of ~500°C. The Mn and Ge effusion cell temperatures were varied from 840 to 1060, and 1180 to 1220 °C, respectively, to systematically change the Mn/Ge flux ratio. The $GeMnN_2$ films were not capped for subsequent *ex situ* studies. Electron-transparent cross-sectional samples, prepared by conventional mechanical polishing and Ar ion milling methods, were characterized by CBED and HRTEM using a Hitachi H9000-NAR microscope operated at 300keV. Composition analysis of the films was done by energy dispersive

spectroscopy (EDS) and by depth profile using x-ray photoelectron spectroscopy (XPS). XAS and XMCD measurements were carried out on beamline 4-ID-C at the Advanced Photon Source. The samples were mounted in a superconducting magnet cryostat with the field along the x-ray beam propagation direction, both 20º above the film plane. The beamline resolution at the Mn *L* edge was set to ~0.27 eV. Data were collected in total electron yield mode by monitoring the sample photocurrent and reversing the photon polarization at each energy point at 5 K in a field of 2 T. Magnetic properties of the material were also characterized with MPMS. The temperature dependences of the magnetization were measured at fields of 100 Oe and 1000 Oe during warming up and cooling down in the temperature range of 2K to 400K, the field dependences of the magnetization were measured at 2K, 5K, 50K, 300K and 400K with magnetic field up to 3 T, respectively.

First-principles calculations used the Full-potential Linearized Augmented Plane Wave (FLAPW) method as implemented in *flair*[15]. For the ideal materials, the calculations were done using the primitive unit cells (either 8 or 16 atoms depending on the structure; see below), while cells up to 128 atoms were used for defect calculations; the calculations included full structural relaxation. The Brillouin zone sampling for the different structures used *equivalent* uniform *k*-point meshes corresponding to a 16×16×16 mesh for cubic zincblende, with tests in each structure corresponding to 24×24×24 to ensure convergence; the energy cutoff for the LAPW basis was 218 eV.

III. Results

Before discussing the growth and characterization of $GeMnN_2$ films, we first present results of spin-polarized GGA density functional calculations of this material. For many of the III-V semiconductors there are two competing phases, the cubic zincblende and the hexagonal

wurtzite. Both of these structures are tetrahedrally bonded, but differ in their relative stacking. ABC_2 semiconductors are obtained by replacing the group III atoms by A and B atoms, leading to an intrinsic lowering of the crystal symmetry. The two competing structures (Fig. 1), now are (*a*) the primitive orthorhombic oP16 structures, and (*b*) the body-centered tetragonal chalcopyrite (tI16). The common chalcopyrite tI16 structure, with 8 atom/unit cell, is derived from the cubic zincblende structure by a doubling of the conventional cubic cell along the *c*-axis, such that the *c/a* ratio is no longer fixed by symmetry. The relationship between the orthorhombic oP16 structure, with 16 atoms/cell, and the hexagonal wurtzite structure (see also Table I) is obtained by noting that a hexagonal lattice can be described as an orthorhombic C-centered lattice, but with a particular *b/a* ratio. Then, because the A and B atoms are distinct, there is both a loss of centering and a doubling, resulting in the oP16 structure. Because of these structural similarities between the tI16 and oP16 structures, and the relationship to the cubic zincblende and hexagonal wurtzite forms found in the AB semiconductors, we compare and contrast the electronic and magnetic properties in the tI16 and oP16 structures.

For ferromagnetic ordering, the orthorhombic structure is calculated to be a zero gap semiconductor with a magnetic moment of 5 μ_B/Mn atom and is favored over the corresponding (slightly half-metallic) chalcopyrite structure. However, as expected from superexchange arguments, AFM ordering is strongly favored in both structures: by 0.44 eV/Mn (0.56 eV/Mn) for the oP16 (tI16) structure. Combined with the large difference of 0.17 eV/atom in the structural energies between the two structures, the calculations clearly predict that the ground state of $GeMnN_2$ is an orthorhombic AFM with the so-called G ordering, in which each Mn spin is antiparallel to its four nearest Mn neighbors; the other distinct AFM orderings consistent with the overall symmetry, the A and C orderings, are less favored by 0.19 and 0.13 eV/Mn, respectively. The local magnetic moment is found to be somewhat less than 5 μ_B/Mn, with the

exact value depending on how the magnetization density is apportioned. The calculated structural parameters (Table I) and magnetic ordering are in excellent agreement with the refined neutron and x-ray derived experimental values first reported in the early 1970s[16,17].

The calculated density of states (DOS) is shown in Fig. 2. As seen from the total DOS, $GeMnN_2$ is an AFM semiconductor, with the Mn atoms forming two magnetic sublattices. At the LDA/GGA level, the calculated gaps are likely underestimated. LDA+U calculations for *U-J* up to 5 eV show an increasing gap, a slight increase in local Mn *d* moment in the atomic sphere, and an increased hybridization of the states near the gap, but no qualitative change in the physics. As an example, the DOS for *U-J* = 4eV are also shown in Fig. 2. The occupied states closest to the Fermi level are Mn-derived, with small admixtures of N and Ge character. The Mn atoms on each sublattice are almost fully polarized, as expected from simple superexchange arguments. In contrast to the prototypical perovskite transition-metal oxides where the path (neglecting direct hopping) connecting two sites with the same spin includes an AFM coupled site, in $GeMnN_2$ such a path can go through any of the 8 Ge atoms without going through one of the 4 opposite spin Mn sites. Thus, electrons of a given spin "see" only half the Mn atoms and can propagate throughout the lattice, suggesting that modifications to one spin sublattice will not have a large effect on the electronic states of the other.

Experimentally, a series of $GeMnN_2$ films (~60 nm thick) were grown with Mn/Ge flux ratios (estimated from vapor pressure data at the growth cell temperatures) of 6-8, unless otherwise specified. (Higher Mn/Ge flux ratios mostly result in clusters on the film surface.) Note that due to the low sticking coefficient of Mn at the growth temperature ~500 ^{o}C, the growth rate, estimated from TEM studies, is only ~7 nm/h. The growth of GaN buffer layers and $GeMnN_2$ thin films was monitored *in situ* by reflection high-energy electron diffraction (RHEED). On MgO(111) and 6H-SiC(0001) substrates, a streaky (1x1) RHEED pattern was observed during

the GaN buffer layer growth, indicating two-dimensional growth and Ga-polar films[18]. On the Al_2O_3(0001) substrate, a (3x3) RHEED pattern was observed, suggesting N-polar GaN buffer layer[18]. Nevertheless, spotty RHEED patterns were observed during the growth of the $GeMnN_2$ layer (Fig. 3(a) inset) on all three substrates, suggesting that the growth has become three-dimensional. This is also confirmed by an atomic force microcopy (AFM) image of the surface morphology of these $GeMnN_2$ films. Shown in Fig. 3(a) is a film grown on a Al_2O_3(0001) substrate, where three-dimensional growth is evident with a RMS roughness of 2.5 nm. Growths on MgO and SiC substrates (with similarly grown GaN buffers) exhibit qualitatively similar behavior, with RMS roughness of 1.6 and 4.4 nm, respectively (see Table II).

The structure of the $GeMnN_2$ films was further characterized by XRD and TEM. Shown in Fig. 3(b) are XRD rocking curves for films grown on Al_2O_3(0001) and MgO(111) substrates, and the full-width-at-half-maximum (FWHM) determined from the rocking curves for films grown on all three types of substrates are summarized in Table II. Clearly, films grown on MgO substrates exhibit higher quality, reflected in a smaller FWHM, consistent with the surface roughness seen by AFM.

Bright field TEM (amplitude contrast) and HRTEM (phase contrast) images are shown in Fig. 4(a, b) for a 60 nm-thick $GeMnN_2$ film grown on a GaN buffer on a MgO(111) substrate. An abrupt interface is seen between the lattice of the $GeMnN_2$ film and that of the GaN buffer layer, which is epitaxial to the MgO(111)[14]. We have also used the stronger electron scattering to look for secondary phases with selected area electron diffraction. No such phases were detected when scanning along the film within the size of the selected area aperture of ~450 nm and within the converged nanoprobe of ~45 nm. In addition, by comparing the experimental convergent beam diffraction pattern (Fig. 4(c)) to those calculated by kinematic diffraction theory for the orthorhombic and tetragonal chalcopyrite structures (Fig. 4(d)), we have determined that the

$GeMnN_2$ film is indeed orthorhombic, consistent with the first-principles calculations. Finally, the following crystallographic orientation relationships are found: $GeMnN_2$(001)||GaN(111)||MgO(111), $GeMnN_2$(100)||GaN(11-2)||MgO(11-2) and $GeMnN_2$ (210)||GaN(01-1)|| MgO(01-1).

We have examined the electronic and magnetic properties of these films by XAS and XMCD at the Mn L edges. The *L* absorption edges probe the $2p \rightarrow 3d$ transitions; hence exciting with circularly polarized radiation, and measuring the differential absorption between parallel and antiparallel photon helicity and sample magnetization, we obtain the magnetic structure of the unoccupied Mn 3*d* states. This differential absorption is related to the average magnetic moment of the 3*d* orbitals.

Figure 5(a) shows the experimental XAS and XMCD spectra (solid curves) of a $GeMnN_2$ film grown on SiC with Mn/Ge flux ratio of 23, taken at the Mn $L_{3,2}$ edge, as well as a fit (dotted curves) to the experimental data. As in Ref. [19], the fit to the XAS data consists of a two-site model: the majority component being a spectrum calculated for Mn^{2+} in atomic multiplet theory [19,20], with a small Mn^0 component derived from experimental XAS data taken from a metallic Mn film. The atomic multiplet calculations were done in O_h symmetry with zero crystal-field splitting. The second component was introduced to improve the agreement with some post-edge XAS intensity noted in one of the films. The metallic component contributes up to ~5.8% of the spectral weight in the Mn/Ge=15 sample (not shown), and less than 2% in all the others. The fit to the XMCD spectra consisted of a pure Mn^{2+} multiplet, with no metallic component, showing that the minority component does not participate in the magnetism. The excellent agreement with these fits clearly indicates that the Mn is divalent. Due to the surface sensitivity of our electron yield measurements, one possibility is that the highly localized Mn^{2+} may be related to a surface oxide phase, similar to that observed on Mn-doped GaAs[21]. However, we note that the Mn^{2+}

component in $GeMnN_2$ is magnetic. If this component were due to a MnO surface oxide layer, it would be antiferromagnetically ordered and we would not expect a measureable XMCD spectrum. We also point out that in Mn-doped GaAs, in addition to Ga substitutions, Mn also exists as a mobile dopant at interstitial sites, and is much more available for bonding to atmospheric oxygen than in the present case of $GeMnN_2$.

In Fig. 5(b), we show the XMCD spectra for four samples grown with different Mn/Ge flux ratio, normalized to the primary L_3 multiplet feature. The XMCD spectra have a high degree of consistency from sample to sample, indicating that the Mn ions that participate in the magnetism have similar bonding configurations. In the inset, we show the average Mn moment plotted vs. Mn/Ge flux ratio. The moments were estimated from the ratio of the coefficients from the multiplet fits to the XMCD spectra to the corresponding Mn^{2+} XAS coefficients, scaled to the expected $5\mu_B$ for a $Mn^{2+}(d^5)$ state. Inspection of this plot reveals that for samples grown with Mn/Ge flux ratio less than 10, the magnetic moments are significantly higher than those grown with higher Mn/Ge flux ratio. Overall, these moments are small, about 0.25 to 0.47 μ_B/Mn, suggesting that there is no direct ferromagnetic coupling between Mn atoms. The moments are likely due to defects and/or impurities, consistent with MPMS observations described below.

Fig. 6(a) presents the temperature (T) dependence of the magnetization (M) of a film grown on MgO substrate. The magnetization shows a rapid and monotonic increase at low temperatures, and is fit excellently by the Curie's law $M = C \cdot \frac{H}{T}$, where C is the Curie constant, H is the applied field. In addition, the magnetic field dependence of the magnetization at different temperatures (2K, 5K, 50K and 400K) (Fig. 6(b)) exhibits no hysteresis and no variation from the Brillouin function[22], confirming that the sample is not ferromagnetic, but rather paramagnetic in nature. We attribute the main contribution of the paramagnetic signal to impurities in the MgO

substrate as the estimated impurity concentration from the Curie constant is about $1x10^{-4}$ atomic ratio to Mg, the same order as the paramagnetic impurities found in MgO substrates[23,24].

On the other hand, although the $GeMnN_2$ thin films grown on SiC and Al_2O_3 substrates showed inferior structural properties, they exhibited starkly different magnetic properties. Fig. 7(a) is the zero-field cool (ZFC) and field cool (FC) magnetization curves measured in an external field of 100 Oe from a $GeMnN_2$ /SiC thin film with a Mn/Ge flux ratio of eight. The dispersion between the ZFC and FC curves persists up to 400K, indicating that a magnetic moment exists and the ferromagnetic transition temperature (T_C) of the film is higher than 400K, the temperature upper limit of the MPMS. To determine the T_C, the magnetization versus temperature curve (Fig. 7(b)) in an external field of 1000 Oe is fitted with the combined Curie-Weiss Law, $M = c * \frac{H}{T} + M_0 * (1 - \frac{T}{T_C})^{\beta}$, in which the magnetization is dominated by paramagnetic behavior at low T, but ferromagnetism at high T. The fit yields a ferromagnetic T_C of 482K with a fitting parameter $\beta = 0.04$ (the red curve in Fig. 7(b)). This is consistent with results obtained from field-dependent magnetizations at various temperatures (Fig. 7(c)), where hysteresis loops with considerable remanence and coercivity persist up to 400 K (Fig. 7(d)). Again, the low temperature paramagnetic behavior is from the paramagnetic impurity of the SiC substrate, which can be estimated similarly as above to be about two orders less than the impurities in the MgO substrate.

Assuming all Mn atoms contribute to the magnetic ordering, a magnetic moment of only 0.34 μ_B/Mn is estimated from the saturation magnetization. This value is much lower than what would be expected if the Mn atoms were ferromagnetically coupled. However, if Mn is antiferromagnetically coupled, as predicted by the first-principles calculations, the moment observed should then be due to defects and/or impurities, e.g., Ge antisites, which exhibit a

moment of 5 μ_B/Ge (see calculations below). In such a case, the concentration of Ge antisites is calculated to be ~3.5%. Note that a factor of 2 is used since Ge antisites should only occupy one of the two sublattices. XPS depth profiling was carried out on a sample grown under similar conditions, which yields a Ge concentration 4.2% higher than Mn, in good agreement with that estimated from the MPMS results. On the other hand, the higher quality of $GeMnN_2$ thin films grown on MgO(111) substrates may indicate an absence (or lower concentration) of defects, and consequently paramagnetic behavior.

IV. Discussions

To elucidate the origin of magnetism found in the $GeMnN_2$ thin films, we note that although the ideal stoichiometric compound is AFM, defects and/or impurities on one Mn sublattice will effectively remove the spin of the Mn without affecting the magnetism of the other sublattice, and result in a net *ferri*magnetic moment for the system. This model of interactions has a number of implications for the magnetic properties: 1) if there are defects/impurities on the Mn sites, the material should show a ferromagnetic-like response, i.e., there should be a hysteresis loop, although it may be difficult to saturate the moment; 2) the net moment should be related to the number of defects/impurities, not the total number of Mn atoms; 3) for Mn-rich conditions, the response should be more paramagnetic due to frustration; and 4) the magnetic response should be sensitive to the presence of impurities, which opens up the possibility of tailoring material properties through the choice of dopants.

To investigate these possibilities, we performed supercell calculations for *i*) a Ge antisite (a likely defect for Ge-rich growth) - on a Mn site, *ii*) an O impurity – whose presence is indicated by XPS depth analysis – on a N site, and *iii*) a Cu impurity, chosen as an example with a different number of *d* electrons on a Mn site. A Ge antisite results in a net ferrimagnetic moment

of 5 μ_B/Ge antisite and a decreased FM-AFM energy difference (~0.31 eV/Mn). Although the DOS is low at the Fermi level (Fig. 8), there are states of both spins. An O impurity has little effect on the Mn moments, although it does induce a small (~0.25 μ_B/O) moment and a metallic behavior at E_F. The Cu impurity behaves similar to the Ge antisite, causing a ferrimagnetic moment of 4 μ_B/Cu. The resulting electronic structure (Fig. 8) is now half-metallic, i.e., semiconducting in the minority spin direction: The states at E_F are fully polarized and, because there are holes in the majority Mn bands, the material is *p*-type.

These results demonstrate that different dopants/impurities place the impurity states and the Fermi level at different positions in the gap, making both *n*- and *p*-type doping possible. Moreover, the defects induce a net (ferrimagnetic) moment into an AFM background, but the carriers can still be spin-polarized. These intriguing results, however, assume that defects will preferentially occupied one magnetic sublattice. To test this assumption we compared the energies of two Cu impurities on the same and different sublattices: In a 128 atom cell, there is a small, but distinct, energy preference of ~0.05 eV for the two Cu atoms to be on the same magnetic sublattice.

These results demonstrate the feasibility of producing spin-polarized carriers and magnetic moments in a semiconductor with an antiferromagnetic background by selectively substituting the magnetic element in a sublattice by defects or impurities. A natural question is the generality of this approach. To address this issue we have carried out calculations for $MnGeAs_2$. Although there are differences in details[25], the overall picture remains the same: there are two weakly interacting AFM Mn sublattices and defects such as Ge antisites and Cu impurities on one Mn sublattice will result in a net ferrimagnetic moment. Similar behavior should be expected in other AFM semiconductors and oxides.

V. Conclusions

In summary, we have synthesized epitaxial orthorhombic $GeMnN_2$ thin films by plasma-assisted MBE. The magnetic properties of the films are related to defects, with samples grown under Ge-rich conditions exhibiting a net magnetic moment above room temperature. These results are explained by first-principles calculations, showing that the preferential substitution of one magnetic sublattice of $GeMnN_2$ by impurities and/or intrinsic defects such as Ge antisites produces a net magnetic moment in an antiferromagnetic background, and also introduces spin-polarized carriers near the Fermi level. Measurements such as temperature and magnetic field dependent XMCD and magnetotransport are needed to further investigate these novel selective-doping induced magnetic properties of $GeMnN_2$.

Acknowledgements:

Work at UWM was supported by the National Science Foundation (DMR-0706359) and U.S. Department of Energy (DE-FG02-06ER46328). Use of the Advanced Photon Source was supported by the U. S. Department of Energy, Office of Science, Office of Basic Energy Sciences, under Contract No. DE-AC02-06CH11357. A portion of this research was conducted at the Center for Nanophase Materials Sciences, which is sponsored at Oak Ridge National Laboratory by the Office of Basic Energy Sciences, U.S. Department of Energy.

Figure Captions:

Fig. 1 (color online) Ball-and-stick model for (a) hexagonal (oP16) and (b) cubic (tI16) $GeMnN_2$.

Fig. 2 (Color online) Calculated majority (↑) and minority (↓) Mn local density of states for AFM orthorhombic $GeMnN_2$. Upper inset: Structural model of the oP16 structure with the Mn spin orientations labeled by arrows. Lower inset: Total DOS. The solid background DOS correspond to LDA+U calculations for U-J = 4 eV.

Fig. 3 (color online) (a) An AFM image of a $GeMnN_2$ film grown on a GaN buffer on a Al_2O_3(0001) substrate (image size: 4x4 μm^2). Inset: a spotty RHEED pattern of taken along the GaN [11-20] direction, indicative of 3D growth. (b) XRD rocking curves of $GeMnN_2$ films grown on MgO(111) and Al_2O_3 (0001) substrates.

Fig. 4 (color online) (a) Bright field TEM of $GeMnN_2$ film (top) grown on GaN buffer layer (middle) on MgO(111) substrate (bottom) with denoted interfacial area of HRTEM lattice image (b) and experimental CBED pattern of the film (c). Note the very top bright band is the vacuum. Comparison with calculated diffraction patterns (d) of orthorhombic $GeMnN_2$ in the [210] zone, and chalcopyrite in the [02-1] zone reveals fit with the orthorhombic phase.

Fig. 5 (Color online) (a) Experimental XAS and XMCD spectra (solid curves) of a $GeMnN_2$ thin film grown on a SiC substrate with a Mn/Ge flux ratio of 23, taken at the Mn $L_{2,3}$ edge at 5 K and 2 T, and calculated spectra (dotted lines) for the Mn^{2+} valence. (b) XMCD of four $GeMnN_2$ films grown with Mn/Ge flux ratios of 23 (blue), 15 (red), 8 (green), and 4 (black).

Fig. 6 (Color online) Magnetic properties of a $GeMnN_2$ thin film grown on a MgO(111) substrate. (a) Temperature-dependence of the magnetization (field cooled in 1000 Oe) with fitting to the Curie-Weiss law. (b) Magnetic field dependence of the magnetization at 2, 5, 50 and 400K.

Fig. 7 (Color online) Magnetic properties of a $GeMnN_2$ thin film grown on a SiC substrate. (a) Temperature-dependence of the magnetization for zero-field cooled and field cooled runs in a 100 Oe magnetic field; (b) field cooled in 1000 Oe with fitting to the Curie-Weiss law. (c) Magnetic field dependence of the magnetization at 2, 5, 50 and 400K and (d) expanded view near zero field at 50 and 400K. As a reference, the field dependence of the SiC substrate at RT and 4K are also plotted in (c) and (d), which indicate a non-ferromagnetic and slight paramagnetic behavior at 298K and 4K, respectively.

Fig. 8 (Color online) Spin-resolved density of states around the Fermi level for a Ge antisite on a Mn site (Ge_{Mn}), an oxygen impurity on a N site (O_N), and a Cu impurity on a Mn site (Cu_{Mn}).

TABLE I. The calculated structural parameters of the oP16 structure compared to the experimental (Ref. [16]) values and to that of an ideal hexagonal arrangement.

	Calculated positions			Experimental positions			Ideal		
	x	y	z	x	y	z	x	y	z
Mn	0.079	0.624	0	0.076	0.615	0	1/12	5/8	0
Ge	0.075	0.124	-0.002	0.076	0.117	-0.008	1/12	1/8	0
N	0.068	0.111	0.361	0.063	0.113	0.356	1/12	1/8	3/8
N	0.094	0.640	0.389	0.098	0.642	0.405	1/12	5/8	3/8

	Calculated lattice parameters	Experimental lattice parameters	Ideal
a	5.497 Å	5.486 Å	
b/a	1.218	1.217	$2/\sqrt{3} \approx 1.155$
c/a	0.953	0.956	$2\sqrt{3}/3 \approx 0.943$

TABLE II. RMS roughness determined from AFM measurements and FWHM from XRD rocking curves.

Substrate	RMS roughness (nm)	Rocking curve FWHM (arcsec)
MgO(111)	1.6	504
Al_2O_3(0001)	2.5	987
6H-SiC(0001)	4.4	612

References:

[1]S. A. Wolf, D. D. Awschalom, R. A. Buhrman, J. M. Daughton, S. von Molnár, M. L. Roukes, A. Y. Chtchelkanova, D. M. Treger, Science, **294.** 1488 (2001).

[2]I. Žutić, J. Fabian, and S. Das Sarma, Rev. Mod. Phys. **76**, 323 (2004).

[3]H. Ohno, Science **281**, 951 (1998).

[4]T. Dietl, H. Ohno, F. Matsukura, J. Cibert, D. Ferrand, Science **287**, 1019 (2000).

[5]S. J. Pearton, C. R. Abernathy, M. E. Overberg, G. T. Thaler, D. P. Norton, N. Theodoropoulou, A. F. Hebard, Y. D. Park, F. Ren, J. Kim, and L. A. Boatner, J. Appl. Phys. **93**, 1 (2003).

[6]C. Liu, F. Yun, and H. Morkoc, J. Mater. Sci.: Mater. Electron. **16**, 555 (2005).

[7]A. H. Macdonald, P. Schiffer, and N. Samarth, Nature Mater. **4**, 195 (2005).

[8]S. Kuroda, N. Nishizawa, K. Takita, M. Mitome, Y. Bando, K. Osuch, and T. Dietl, Nature Mater. **6**, 440 (2007).

[9]T. Dietl, Nature Mater. **9**, 965 (2010).

[10]S. C. Erwin and I. Zutic, Nature Materials **3**, 410 (2004).

[11]S. Cho, S. Choi, G. –B. Cha, S. C. Hong, Y. Kim, Y. –J. Zhao, A. J. Freeman, J. B. Ketterson, B. J. Kim, and Y. C. Kim, Y. C, Phys. Rev. Lett. **88**, 257203 (2002).

[12]P. Mahadevan and A. Zunger, Phys. Rev. Lett. **88**, 047205 (2002).

[13]Y. Cui and L. Li, Appl. Phys. Lett. **80**, 4139 (2002).

[14]V. K. Lazarov, J. Zimmerman, S. H. Cheung, L. Li, M. Weinert, and M. Gajdardziska-Josifovska, Phys. Rev. Lett. **94**, 216101 (2005).

[15]E. Wimmer, H. Krakauer, M. Weinert, and A. J. Freeman, Phys. Rev. B **24**, 864 (1981); M. Weinert, E. Wimmer, and A. J. Freeman, Phys. Rev. B **26**, 4571 (1982); M. Weinert, G. Schneider, R. Podloucky, and J. Redinger, J. Phys.: Condens. Matter **21**, 084201 (2009).

[16]J. Guyader, M. Maunaye, and J. Lang, C. hebd Seanc. Acad. Sci. Paris **272c**, 311 (1971).

[17]M. Maunaye, R. Marchand, J. Guyader, Y. Laurent, and J. Lang, Bull. Soc. Franc. Miner. Crist. **94**, 561 (1971); M. Wintenberger, J. Guyader, and M. Maunaye, Solid State Commun. **11**, 1485 (1972).

[18]A. R. Smith, R. M. Feenstra, D. W. Greve, M.-S. Shin, M. Skowronski, J. Neugebauer, and J. E. Northrup, Appl. Phys. Lett. **72**, 2114 (1998).

[19]D. J. Keavney, S. H. Cheung, S. T. King, M. Weinert, and L. Li, Phys. Rev. Lett. **95**, 257201 (2005).

[20]G. van der Laan and B. T. Thole, Phys. Rev. B **43**, 13401 (1991).

[21]D. Wu, D. J. Keavney, R. Wu, E. Johnston-Halperin, D. D. Awschalom, J. Shi, Phys. Rev. B **71**, 153310 (2005).

[22]Robert C. O'Handley, *Modern magnetic materials: principles and applications* (Wiley, 2000).

[23]R. P. Borges, W. Guichard, J. G. Lunney, J. M. D. Coey, and F. Ott, J. Appl. Phys. **89**, 3868

(2001).

[24]H. Zama, Y. Ishii, H. Yamamoto, and T. Morishita, Jap. J. Appl. Phys. **40**, L465 (2001).

[25]The calculated ground state is an AFM chalcopyrite structure, although the energy difference between the tI16 and oP16 structures is only 0.012 eV/atom and the FM-AFM difference is ~0.06 eV/Mn. The calculated gaps in $GeMnAs_2$ are smaller than in $GeMnN_2$, but as common for density functional calculations, the calculated gaps are expected to be underestimates.

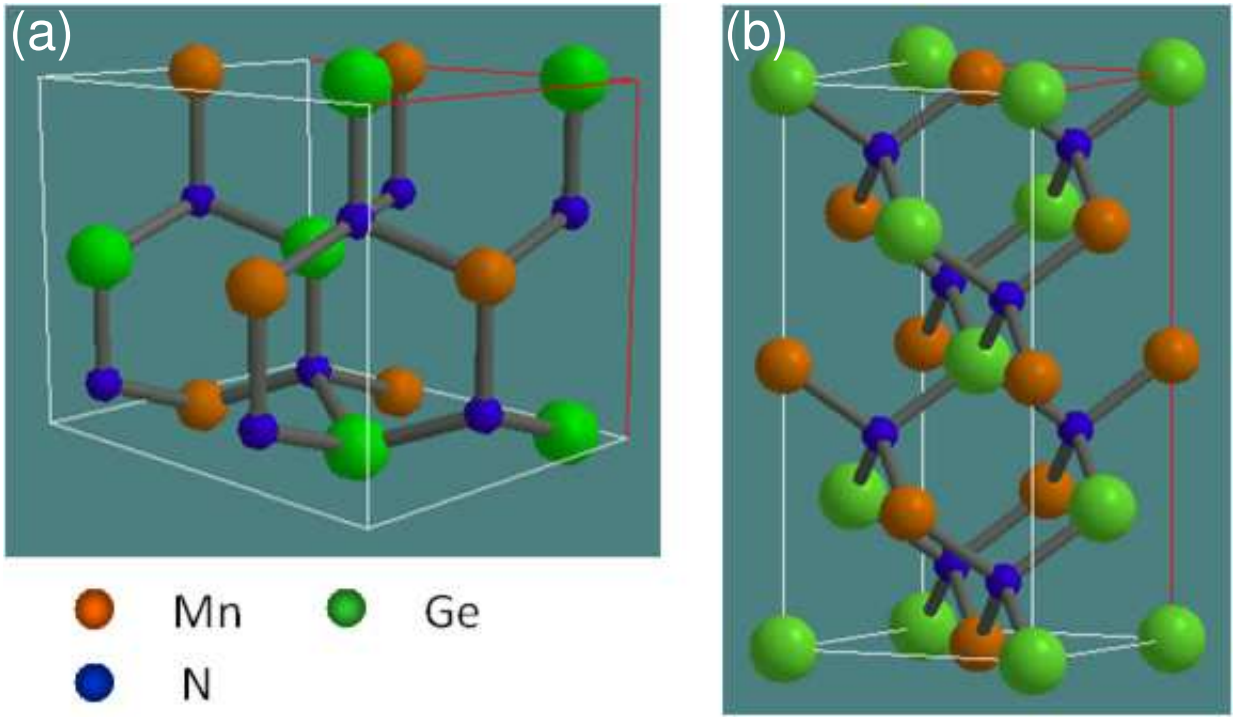

Figure 1 BK11477 06APR2012

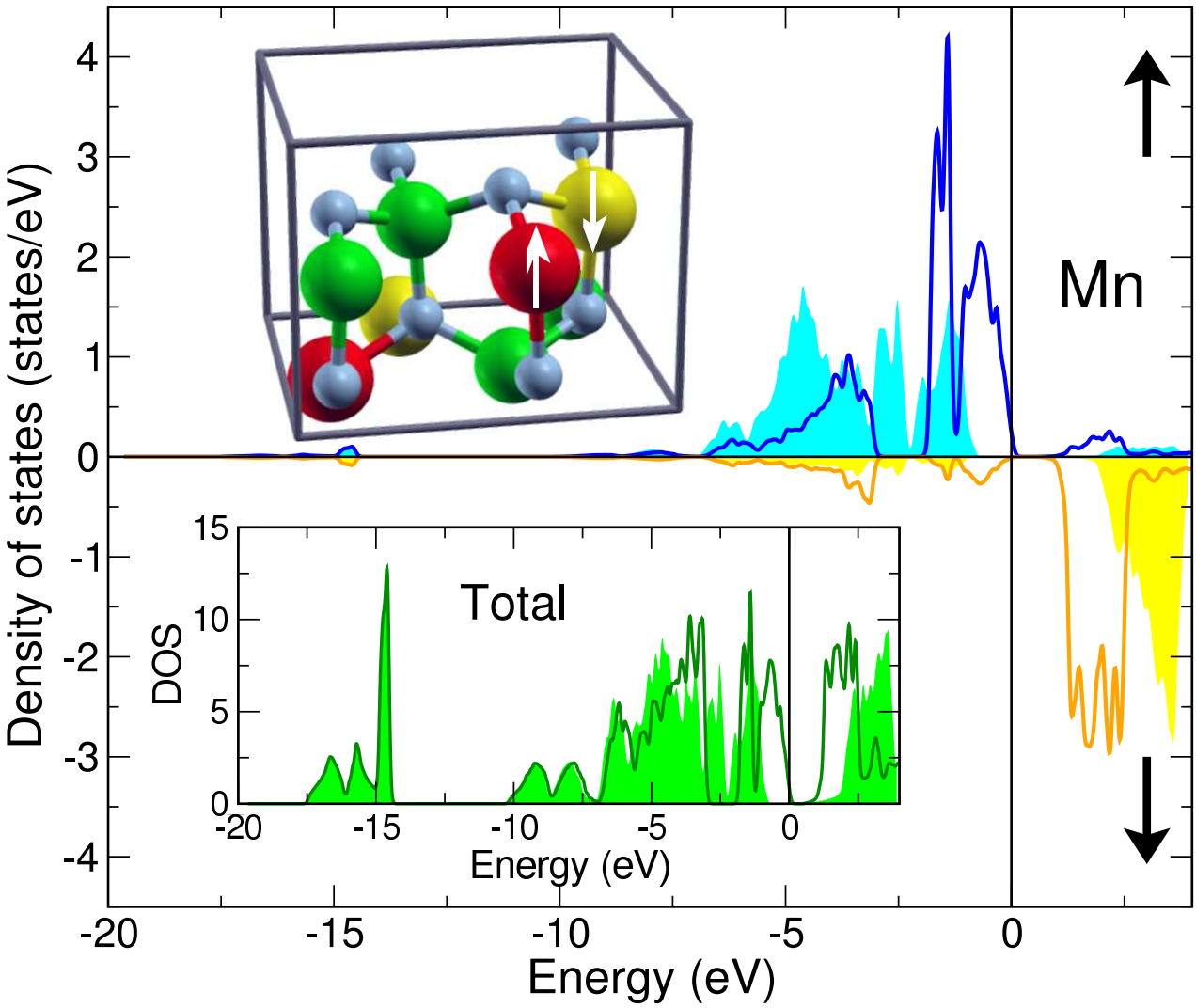

Figure 2 BK11477 06APR2012

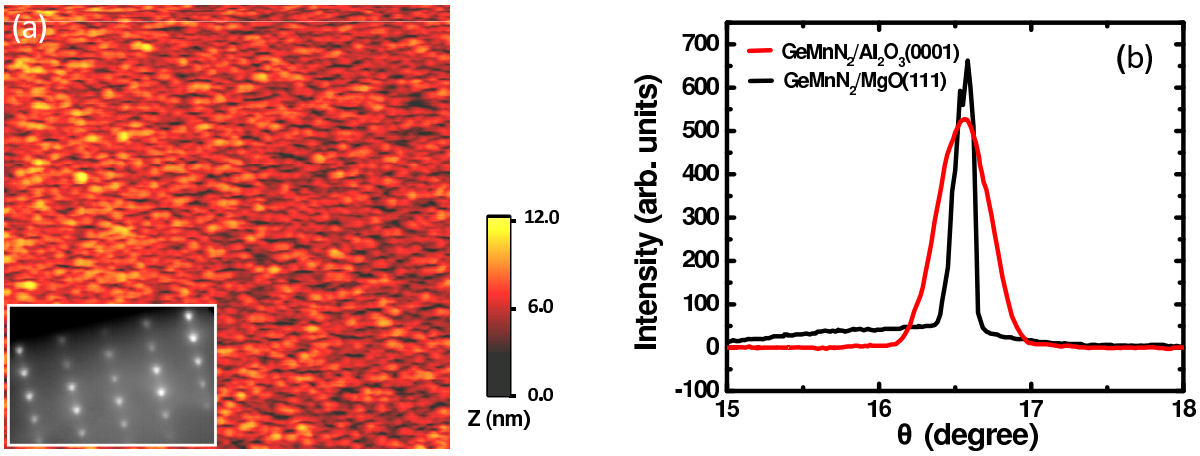

Figure 3 BK11477 06APR2012

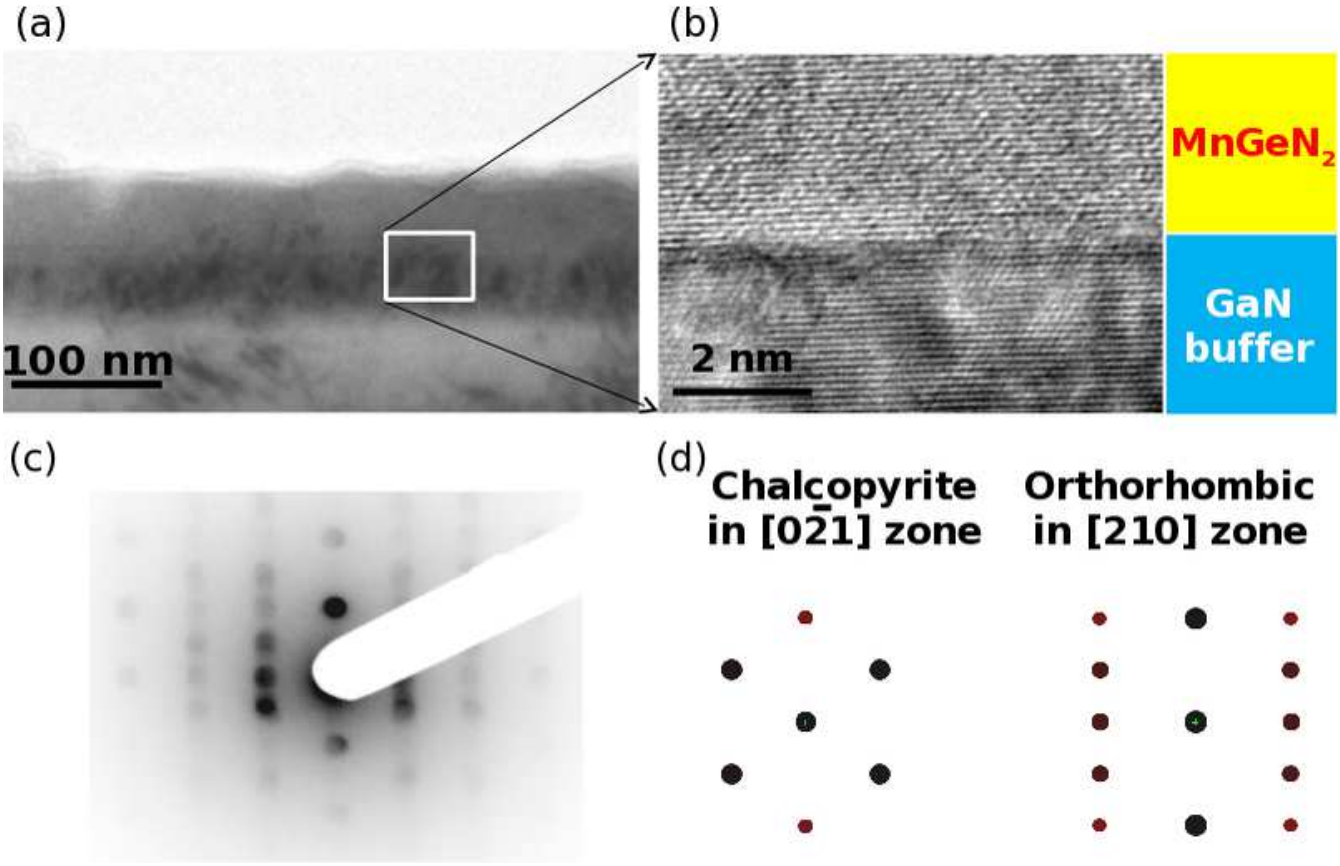

Figure 4 BK11477 06APR2012

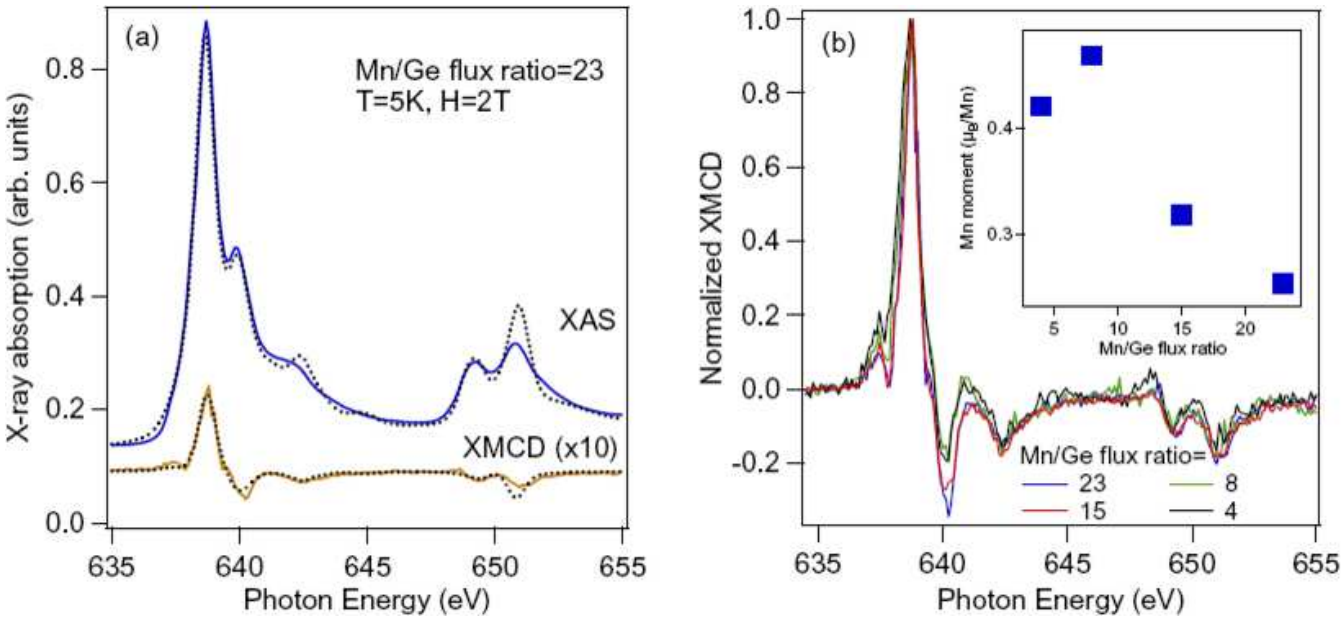

Figure 5 BK11477 06APR2012

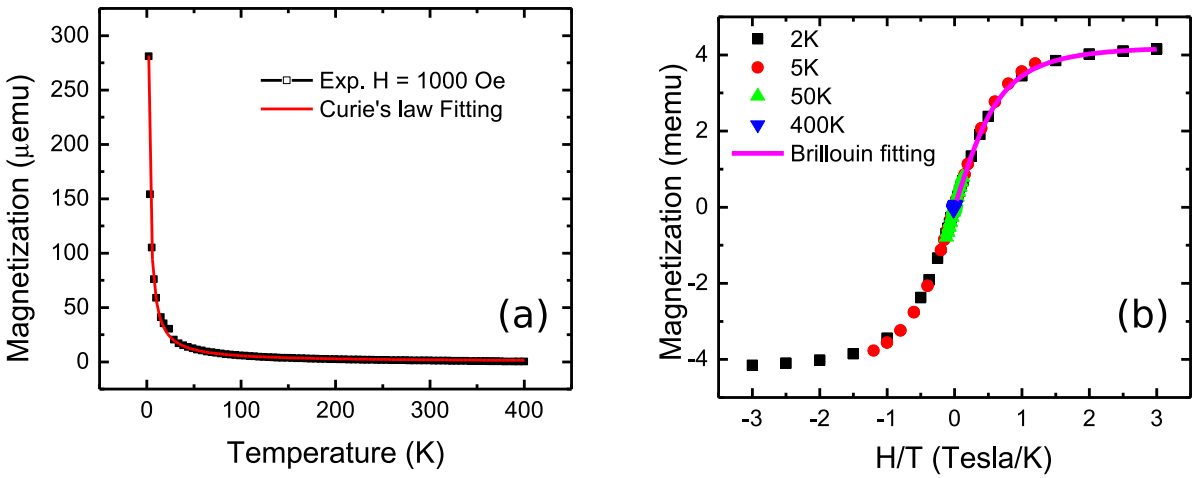

Figure 6 BK11477 06APR2012

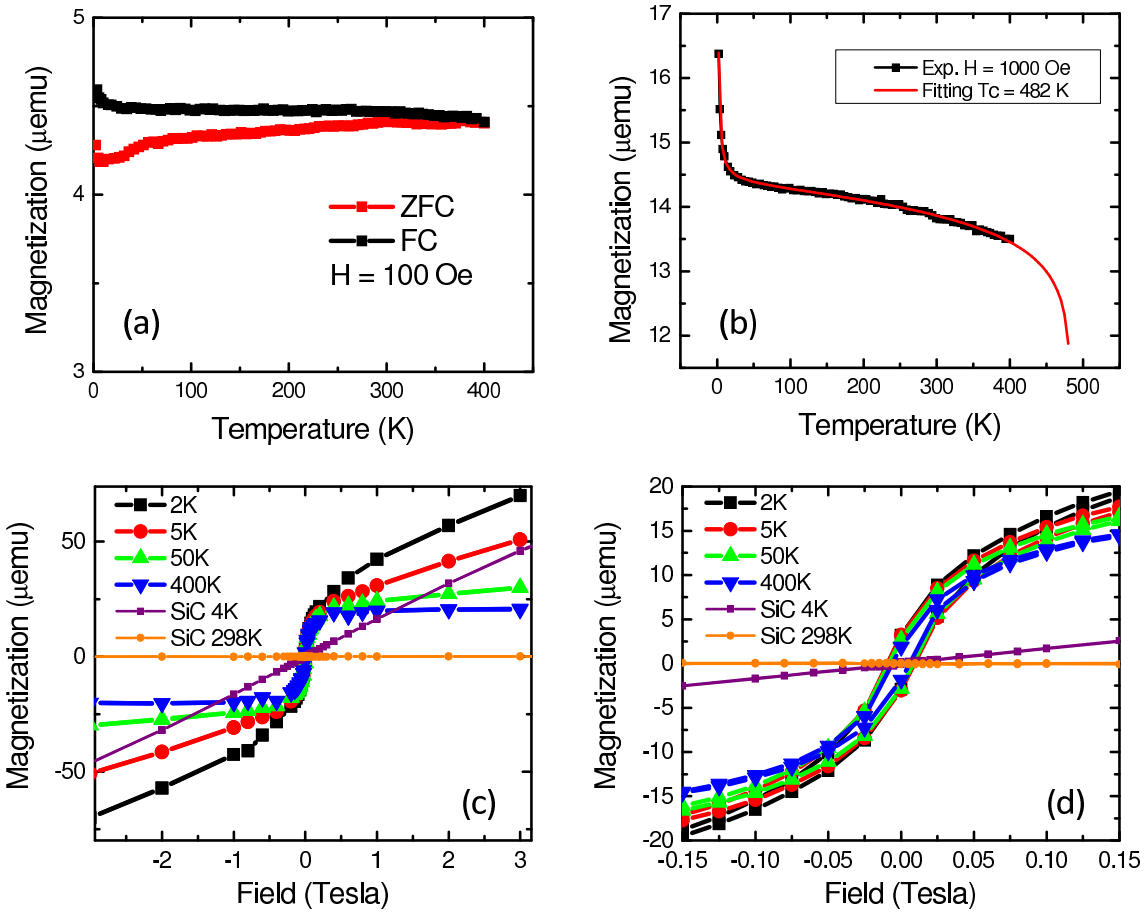

Figure 7 BK11477 06APR2012

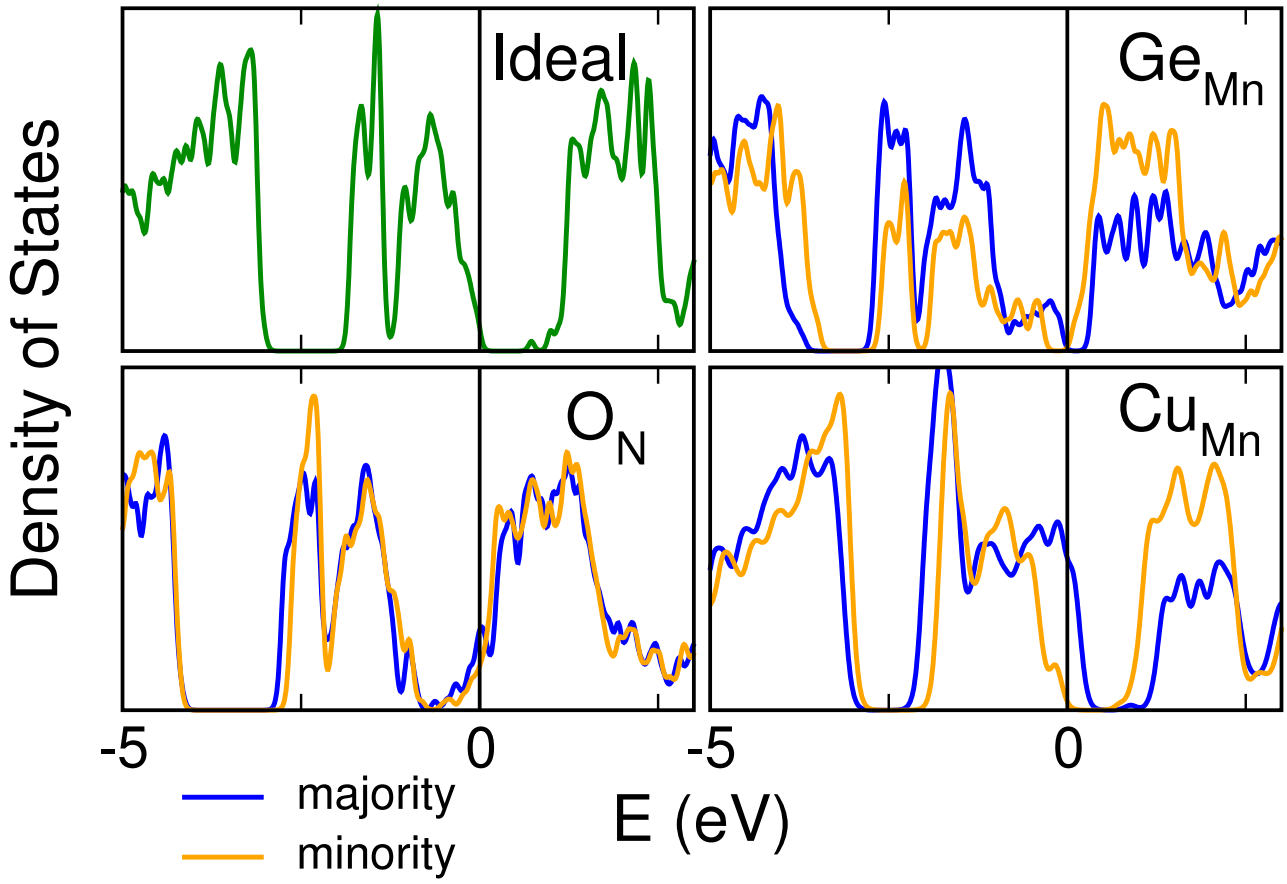

Figure 8 BK11477 06APR2012